Research of TE behaviour and compression property of porous Ni–Al–Cr intermetallic compounds in the β phase region

N.B. When citing this work, cite the original published paper.

(article starts on next page)

Research of TE behaviour and compression property of porous Ni−Al−Cr intermetallic compounds in the β phase region

Yang Yu [a], Baojing Zhang [a,**], Xiaoping Cai [b], Zhejian Cao [c],
Farid Akhtar [d], Xinyang Jiao [e], Xueding Chai [f], Peizhong Feng [a,*]

[a] School of Materials Science and Physics, China University of Mining and Technology, Xuzhou, 221116, PR China
[b] School of Materials Science and Engineering, Tsinghua University, Beijing 100084, China
[c] Division of Systems and Synthetic Biology, Department of Biology and Biological Engineering, Chalmers University of Technology, 41296 Gothenburg, Sweden
[d] Division of Materials Science, Department of Engineering Sciences and Mathematics, Luleå University of Technology, SE-971 87, Luleå, Sweden
[e] School of Mechanical and Electrical Engineering, Suqian College, Suqian, 223800, PR China
[f] School of Mechanical and Electrical Engineering, China University of Mining and Technology, Xuzhou, 221116, PR China

ARTICLE INFO

ABSTRACT

Ni−Al−Cr alloys in the β phase (B2−NiAl) region exhibit remarkable stability and mechanical property. Through thermal explosion (TE) reaction, Ni−Al−Cr intermetallic compounds with high porosity can be obtained. In this study, the focus lies on analyzing the macroscopic morphology, microstructure, phase distribution, TE behaviour, and the mechanical property of porous Ni−Al−Cr in the β phase region. Following the TE reaction, the Al-rich sintered product demonstrates a uniform phase composition and high porosity, reaching 44.39%. The vigorous TE reaction promotes the formation of interconnected pores, while the high porosity structure compromises the mechanical properties of the sample. Conversely, the Al-poor sintered product, due to a moderate TE reaction and low porosity structure, maintains its complete morphology and exhibits excellent compression resistance (yield stress reaching 538 MPa). This study offers valuable insights for the fabrication of porous Ni−Al−Cr materials with exceptional structure and performance.

1. Introduction

Recently, the massive combustion of coal resources and the continuous decline of air quality have pushed researchers to vigorously study the high-temperature gas purification device [1—3]. Due to high porosity, oxidation resistance, thermal shock and high-temperature stability, porous materials can filter the dust and absorb high-temperature harmful gas effectively [4—7]. They show a potential application prospect in high-temperature

---

flue gas filtration. However, a three-dimensional porous structure reduces the strength of the porous materials, and they inevitably face the dilemma of weak mechanical properties [8–10].

Due to high porosity (over 40%) and melting point (1638 °C), excellent thermal conductivity and corrosion resistance, porous Ni–Al–Cr intermetallic compounds have received extensive attention [11,12]. While poor toughness, plasticity, low high-temperature strength, and ease to melt and deformation are their inherent shortcomings, limiting their further application [11,12]. Cr is a commonly used alloying element to improve mechanical properties and oxidation resistance [13–15]. Compared with other Ni–Al–Cr alloys, the sample in the β phase region has a lower density and higher melting point [16–18]. During reaction process, Cr can occupy the vacancy of the Ni atom to form NiAl(Cr) substitutional solid solution [18,19]. Besides, Cr can significantly improve mechanical properties in Ni–Al–Cr alloys through solution strengthening and fine-grain strengthening [20–22]. Our previous work studied the effect of Cr on thermal explosion (TE) behaviour and antioxidant performance in porous Ni–Al–Cr intermetallic compounds. The results indicated that the samples in the β phase region have high porosity structure and excellent oxidation resistance at 900 °C [18]. Presently, the β phase region research mainly focuses on the formation mechanism and interdiffusion effect [16,17]. The TE reaction mechanism and mechanical property of porous Ni–Al–Cr intermetallic compounds remain unclear.

Currently, porous Al-based intermetallics can be prepared by several methods, such as powder metallurgy, melt foaming, self-propagating high-temperature synthesis, etc. [23–28]. TE reaction method is a crucial sintering technology to prepare porous Al-based materials, which has the characteristic of time and energy-saving, simple preparation process. Green compacts can be heated evenly in the tube furnace during the TE reaction, and porous intermetallics with complete morphology and stable pore structure can be achieved [29–31]. In Ni–Al system, severe eutectic reaction between $NiAl_3$ and Al on the surface of Ni particles, releasing a large amount of heat, which is the mechanism of TE reaction [18,29]. Up to now, porous Ni–Al, Cu–Al, Nb–Al, and Ti–Al intermetallics have been synthetized successfully by TE reaction [11,31–33].

In this work, porous Ni–Al–Cr materials were synthesized using the TE reaction method. The main focus of the research was to investigate the TE behavior and compression properties of samples in the β phase region. Furthermore, the Miedema thermodynamic theorem formula was utilized to predict the sequence of phase formation in the binary system. Additionally, the Barsen equation was employed to establish the relationship between porosity and compressive strength. This work provides a primary theoretical foundation for investigating the TE behavior and mechanical properties of porous Ni–Al–Cr intermetallic compounds.

2. Materials and experimental methods

2.1. Component design

Based on the aluminum content, the β phase region was divided into two parts: the Al-rich region and the Al-poor region, as illustrated in Fig. 1. Six different compositions within the β phase region were selected as the research subjects, namely S1 ($Ni_{37}Al_{55}Cr_8$), S2 ($Ni_{43}Al_{57}$), S3 ($Ni_{42}Al_{53}Cr_5$), S4 ($Ni_{54}Al_{34}Cr_{12}$), S5 ($Ni_{63}Al_{37}$), and S6 ($Ni_{52}Al_{43}Cr_5$). Among these samples, S3 and S6 were the primary objects of study, while S1, S2, S4, and S5 served as reference samples.

2.2. Raw materials and preparation process

Fig. 2(a–c) displays the micromorphology of Ni powders (Shanghai Aladdin Biochemical Technology Co., Ltd, 75 μm, 99.9% purity), Al powders (Shanghai Aladdin Biochemical Technology Co., Ltd, 38–75 μm, 99.9% purity), and Cr powders (Shanghai Aladdin Biochemical Technology Co., Ltd, 10 μm, 99.5% purity). The Ni and Cr particles exbihit irregular shapes, while the Al particles appear ellipsoidal and spherical. In Fig. 2(d–f) and Fig. S1, the micro-topography and elemental distribution of the green compact in the β phase region is shown. The Ni phase (light grey), Al phase (black), and Cr phase (dark grey) are uniformly distributed, which promotes the uniformity of phase distribution during the subsequent reaction process. Due to the size difference between the raw powders, some interstitial pores exist at the boundary of different phases [34].

To eliminate the Al_2O_3 layer formed on the surface of Al particles at room temperature, the Al powders were subjected to a heat treatment at 200 °C for 30 min in a tube furnace (OTF-1200X, China) under a hydrogen atmosphere. The three powders were then proportionally mixed using a roller mixer (Mixer-RM1, 100 rpm for 12 h) based on the atomic ratio of $Ni_{37}Al_{55}Cr_8$ (S1), $Ni_{43}Al_{57}$ (S2), $Ni_{42}Al_{53}Cr_5$ (S3), $Ni_{54}Al_{34}Cr_{12}$ (S4), $Ni_{63}Al_{37}$ (S5), and $Ni_{52}Al_{43}Cr_5$ (S6). Subsequently, a cylindrical

Fig. 1 – The experimental ternary phase diagram for the Ni–Al–Cr system at 1000 °C. They are indicated in different colours according to Al content. The orange part stands for the Al-rich region, blue part for the Al-poor region. S1, S2 and S3 are in the Al-rich region. S4, S5 and S6 are in the Al-poor region. Among them, S3 and S6 are the main research objects.
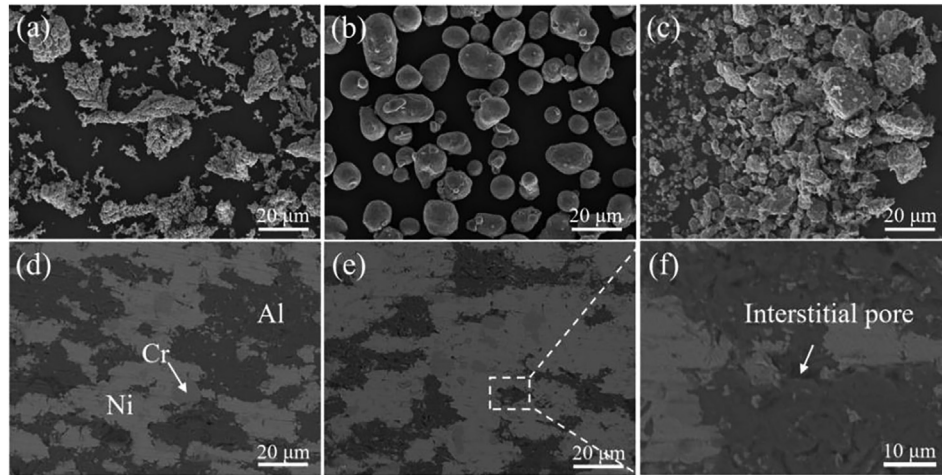
Fig. 2 – (a–c) The micro-topography of the raw powders of Ni, Al, and Cr. (d, e) Low-magnification cross-section micrographs of the green compact of S3 and S6. The black part stands for Al particles, the dark grey part for Cr particles, and the light grey part for Ni particles. (f) High-magnification SEM image of white frame in Fig. 2e.

green compact with a width of 15 mm and a height of 1~2 mm was formed by pressing the mixture using an infrared electric tablet press (DY-30, Shanghai Xinnuo Instrument Equipment Co., Ltd) at a pressure of 300 MPa for 3 min. Under a hydrogen atmosphere, the green compacts were heated to 550 °C and held at that temperature for 30 min. This step, known as the pre-heating stage, is crucial for maintaining the complete morphology of the product [23,29]. Subsequently, the temperature was directly raised to 1000 °C. After holding at 1000 °C for 2 h, the heating was stopped, and the samples were removed from the tube furnace once they reached room temperature. The heating procedure and corresponding real-time images can be observed in Fig. 3.

During the compression test, the Ni–Al–Cr green compact was compressed to a height of 20 mm and a width of 15 mm. After undergoing the heating procedure as described in Fig. 3, the porous Ni–Al–Cr cylindrical samples were subjected to compression testing using an electronic universal testing machine (UTM 5305, China). The loading speed was set at 0.2 mm min^{-1}, and the corresponding data were recorded using the MaterialsTest 5.0 software. To ensure the accuracy of the experimental results, three cylindrical samples with similar dimensions were tested, and the average of the three tests was taken to determine the compressive strength.

2.3. Materials characterization

According to formula (1), the porosity of porous Ni–Al–Cr samples can be determined using the Archimedes drainage method [31,35,36].

$$\theta = (M_2 - M_1) / \rho_0 V \times 100\,\% \qquad (1)$$

θ represents the porosity of the sample, M_1 corrosponds to the weight of the sample when it exposed to air, while M_2 represents the weight of the sample when it is completely immersed in the vacuum pump oil for 24 h. V denotes the sample volume, and ρ_0 is the density of the vacuum pump oil,

which is 0.9 g cm^{-3} [31,35,36]. To measure the time-temperature curves, a self-made temperature measuring device was employed, and visual images were captured using a digital camera (HDR-CX900E, Sony). The device diagram can be seen in Fig. S2. The released heat and thermal effect analysis during the TE process were conducted using a differential scanning calorimeter (DSC, F5-Jupiter STA449, Netzsch, Germany). The DSC experiment was carried out under a stable and continuous argon atmosphere to prevent oxidation. The crystal structure of the sintered and cylindrical products was examined using X-ray diffraction (Bruker D8 Advance, using Cu target with $\lambda = 0.154$ nm). Element identification and microstructure characterization were performed using a field-emission scanning electron microscope (FE-SEM, SU8220, Japan) equipped with Energy Dispersive Spectroscopy.
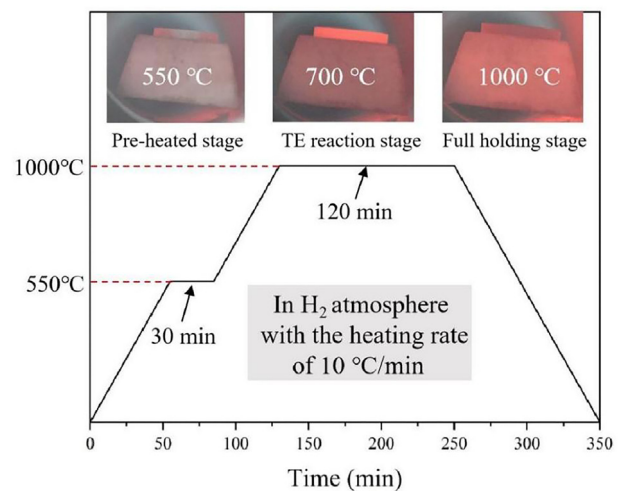
Fig. 3 – The heating procedure and real-time images of porous Ni–Al–Cr intermetallic compounds during TE reaction.

Table 1 — Parameters for the enthalpy energy calculations of Ni—Al—Cr system [37,38].

Elements	Φ	$n_{ws}^{1/3}$	V	P	Q	μ	Q/P	R/P	G	K
	(V)	(cm^{-1})	(cm$^3\cdot$mol^{-1})	(kJ$\cdot$V$^{-2}\cdot$cm^{-1})	(kJ$\cdot$V^{-1})				(10^{10}N$\cdot$m^{-2})	(10^{10}N$\cdot$m^{-2})
Ni	5.2	1.75	6.5	10.6	99.6	0.03	0.10642	0	7.6	18
Al	4.2	1.39	9.9	10.6	99.6	0.07	0.10642	0	2.6	7.6
Cr	4.65	1.73	7.1	10.6	99.6	0.06	0.10642	0	11.5	16

3. Results and discussion

3.1. Thermodynamic calculation of binary phases in Ni—Al—Cr system

Based on the research findings of Agbedor [37] and Shirani Bidabadi [38], the enthalpy energy of binary compounds (Ni—Al, Ni—Cr, Cr—Al) within the Ni—Al—Cr system can be determined using the Miedema thermodynamic theorem. The formation enthalpy energy of the crystalline solid solution containing elements A and B is represented by formula (2) [37,39]:

$$\Delta H_{A \text{ in } B}^{crys} = \Delta H_{chem} + \Delta H_{elas} + \Delta H_{struc} \qquad (2)$$

The ΔH_{chem} represents the chemical contribution of enthalpy energy of the original atomic bond breaking and new components forming. ΔH_{elas} stands for the elastic mismatch energy in the crystalline. ΔH_{struc} is the enthalpy energy required to maintain lattice structure stability. In general, ΔH_{struc} has a weak impact on ΔH_{crys} A in B, and the value of ΔH_{struc} can be set as 0 [37,40]. formula (2) is transformed into formula (3).

$$\Delta H_{A \text{ in } B}^{crys} = \Delta H_{chem} + \Delta H_{elas} \qquad (3)$$

The ΔH_{chem} for each of the binary components can be calculated by the semi-empirical model of Miedema, shown in formula (4) [37]:In formula (4), the $f_{A \text{ in } B}$ is the concentration of

Fig. 4 — The formation enthalpy of binary phases of Ni—Al, Ni—Cr and Cr—Al in the Ni—Al—Cr system.

component A entered in component B. The $\Delta E_{A \text{ in } B}$ and $\Delta E_{B \text{ in } A}$ are shown in formula (7), where K is the bulk moduli of the element, and G stands for the hear moduli.

$$\Delta H_{elas} = x_A x_B \times (x_A \times \Delta E_{BinA} + x_B \times)\Delta E_{BinA} \qquad (6)$$

$$\Delta E_{AinB} = \frac{2K_A G_B \times (V_B - V_A)}{3K_A G_B + 4G_B V_A} . \Delta E_{BinA} = \frac{2K_B G_A \times (V_A - V_B)}{3K_B G_A + 4G_A V_B} \qquad (7)$$

$$\Delta H_{A \text{ in } B} = f_{A \text{ in } B} \times \frac{x_A \times [1 + v_A x_B \times (\varphi_A - \varphi_B)] \times [1 + v_B x_A \times (\varphi_B - \varphi_A)]}{x_A V_A^{\frac{2}{3}} \times [1 + v_A x_B \times (\varphi_A - \varphi_B)] + x_B V_B^{\frac{2}{3}} \times [1 + v_B x_A \times (\varphi_B - \varphi_A)] + x_B} \qquad (4)$$

adjacent atoms in a solid solution, and the calculation formula of $f_{A \text{ in } B}$ is shown in formula (5):

$$f_{A \text{ in } B} = \frac{2PV_A^{2/3}V_B^{2/3}}{n_{wSA}^{-1/3} + n_{wSB}^{-1/3}} \times \left[- (\varphi_B - \varphi_A)^2 + \frac{Q}{P} \right.$$
$$\left. \times \left(n_{wSA}^{1/3} + n_{wSB}^{1/3} \right)^2 - \alpha \times \frac{R}{P} \right] \qquad (5)$$

x_A and x_B represent the molar fraction of components A and B, n_{ws} represents the electronic density at the Wigner-Seitz cell boundary of the constituent elements, φ represents the work function of the constituent elements. V_A and V_B are the molar volumes of components A and B. Besides, α, μ_A, μ_B, Q, P, Q/P and R/P are semi-empirical parameters, confirmed in previous studies [41,42].

The ΔH_{elas} can be written in formula (6). Significantly, the $\Delta E_{A \text{ in } B}$ stands for the elastic mismatch energy, caused by

Relevant parameters of the Ni—Al—Cr system are shown in Table 1. For each binary component, the sum of binary mole fractions is 1 ($x_A + x_B = 1$). The calculation results of the heat of the formation of binary compounds in the Ni—Al—Cr system are shown in Fig. 4.

According to the research findings of Agbedor [37], it is observed that the larger the enthalpy energy of the binary phase, the easier it is to form the corresponding compound. From Fig. 4, the enthalpy energy of Ni—Al and Cr—Al is larger than Ni—Cr. This indicates that the formation of Ni—Cr phase is more challenging. Comparing Cr—Al with Ni—Al, the enthalpy energy of Ni—Al is slightly higher. Therefore, during the TE reaction, the formation of Ni—Al compounds takes priority. In our previous work, we utilized the effective Heat of Formation (EHF) model to calculate the order of formation of different phases in the binary system, and the results are consistent [18].

3.2. The TE behaviour in the β phase region

In the TE mode, when the temperature exceeds the melting point of Al (660 °C), the liquid Al can undergo a violently with Ni and Cr, resulting in the formation of numerous pores [30]. The high porosity structure weakens the binding force between particles, leading to volume expansion [43]. Fig. 5 illustrates the expansion rate and porosity of the sintered products. All samples exhibit relatively high porosity (above 33%) and significant volume expansion (above 18%). In comparison to the Al-poor samples, the Al-rich samples demonstrate higher porosity and a more pronounced expansion effect, indicating a more violent TE reaction in the Al-rich samples. High porosity Ni–Al–Cr intermetallics can be obtained in the Al-rich region. However, it should be noted that compared to the Al-poor sample, the Al-rich sample is more prone to melting and deformation during the TE reaction. The real-time reaction process of the samples can be observed in Video 1 and Video 2. Therefore, excessive doping of Al powder in raw materials should be avoided.

To determine the maximum temperature reached during the TE reaction of the porous Ni–Al–Cr intermetallics, a temperature measuring device was employed to record the real-time temperature. Fig. 6 depicts the time-temperature curves of S3 and S6, with the corresponding visual image capturing the peak state of S3 and S6. As the temperature approaches 700 °C, the sample ignites and undergoes a rapid increase in temperature. The peak temperature can reach nearly 1000 °C, indicating a combustion state. It is observed that S3 can attain a higher peak temperature compared to S6, demonstrating that the TE reaction is more intense in the Al-rich sample.

To further investigate the thermal effects of the TE reaction, a thermal analysis experiment was conducted. Fig. 7 presents the DSC curves of the porous Ni–Al–Cr sample as it was heated from room temperature to 800 °C, with a heating rate of 10 °C min^{-1}. Two exothermic peaks are observed in the temperature range of 600–650 °C. The first peak corresponds
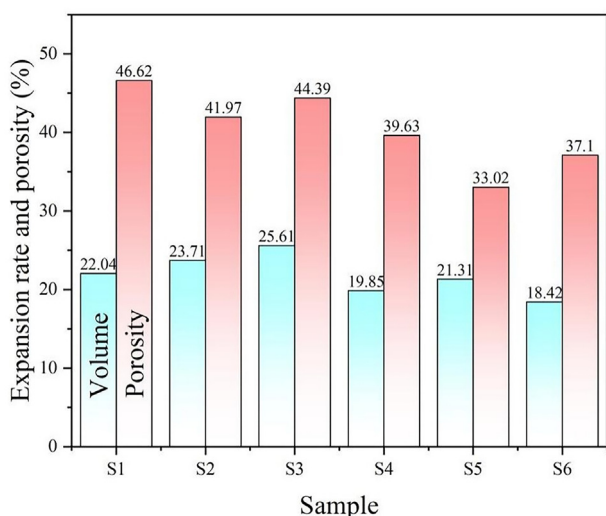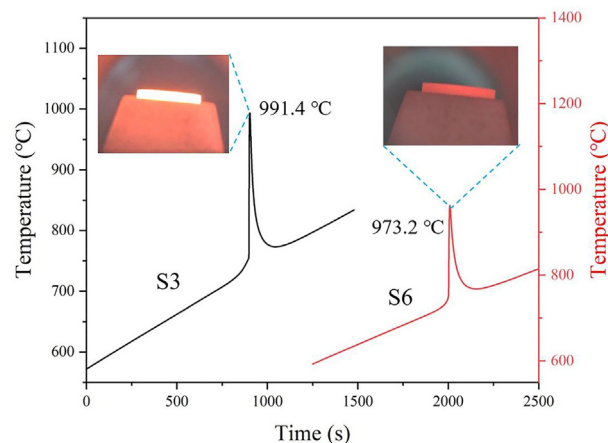
Fig. 6 – The time-temperature curves and visual images of S3 and S6.

to the heat released during the slow diffusion reaction between the elements. It exhibits a gentle shape and relatively weak peak intensity. The second peak corresponds to the violent TE reaction between the Ni and Al elements, characterized by high power features and a narrow temperature range [11,29]. In the Al-rich sample, the violent TE reaction instantaneously releases a significant amount of heat, surpassing that of the Al-poor sample. Specifically, S3 exhibits a heat release amount of 1575 J g^{-1}, whereas S6 only reaches 1378 J g^{-1}. In the Ni–Al–Cr system, the heat release amount from the Cr–Al reaction is lower than that of the Ni–Al reaction [44]. The presence of the Cr element facilitates the TE reaction at a lower temperature and reduces the overall heat release in the Ni–Al–Cr system, thereby mitigating the risk of melting and deformation [23].

Fig. 8(a) illustrates the phase composition of the porous Ni–Al–Cr samples in the β phase region. The predominant phase in the sintered products is the NiAl phase (β phase), and the intensity of the main peaks decreases as the samples transition from Al-rich to Al-poor compositions. Additionally, a small number of other phases are detected, including Ni_2Al_3, Ni_3Al, and $AlCr_4$ phases. In the Ni–Al–Cr system, the atomic radius of Ni (124 p.m.) is close to that of Cr (127 p.m.) [18,44]. During the TE process, Cr atoms can replace Ni atoms, resulting in the formation of a displacement solid solution of NiAl(Cr). The reaction process is depicted in Fig. 8(b). Al-rich samples exhibit a pronounced and complete TE reaction, leading to a uniform phase composition of NiAl. On the other hand, Al-poor samples display a more complex phase composition due to weaker TE reactions and prominent diffusion reactions. Notably, the (110) peak of the sample containing Cr tends to shift to a lower angle, indicating a gradual increase in the crystal plane spacing between Ni and Al as a result of the presence of Cr.

Rietveld refinement of the acquired XRD spectra of S3 and S6 is carried out through the GSAS-II software. The refinement is finished by extracting a structural phase model from a matching reference pattern calculated by the Inorganic Crystal Structure Database (ICSD). A structural model of the NiAl (B2–NiAl, PDF#65–0431, Primitive Cubic, Space group Pm-3m,
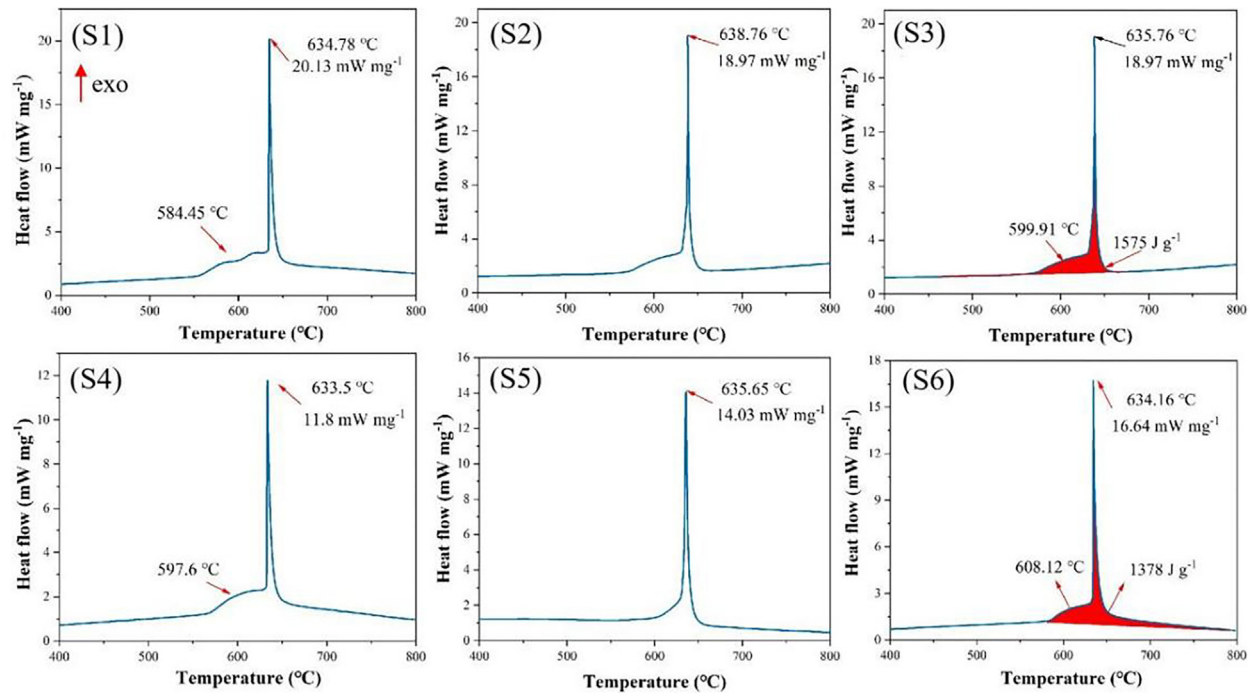

Fig. 5 – The volume expansion rate and porosity of the porous Ni–Al–Cr materials in the β phase region.

Fig. 7 − The DSC curves of porous Ni−Al−Cr samples. The red part represents the heat released per unit mass. (For interpretation of the references to colour in this figure legend, the reader is referred to the Web version of this article.)

a = 0.2877 nm, Code: 58,037) is chosen as the origin position. After respective structural refinement, the result is obvious, shown in Fig. 9. Based on the least-square profile of R-factors, the results of peak shape, position, structure, and background are quantitatively calculated. The corresponding parameters are shown in Table 2. According to Table 2, the values of R_{wp} and χ^2 meet the standard of Rietveld refinement. However, the peak shapes still have drawbacks. These drawbacks may be due to some mesophases in the Ni−Al−Cr substitutional solid solution. Significantly, the χ^2 value of S3 is 1.99, lower than that in S6, which proves that the composition of the sintered product in the Al-rich region is uniform β phase [45].

To investigate the microstructure of the porous Ni−Al−Cr intermetallics in the β phase region, SEM analysis is conducted on the fracture surface, as shown in Fig. 10. All samples show evenly distributed foam structure. Three kinds of pores are observed in porous Ni−Al−Cr: (1) connecting TE pores, (2) closed pores, and (3) micropores [11,30,46]. When the temperature reaches the melting point of Al (660 °C), Al transitions from a solid state to a liquid state, resulting in the formation of connecting TE pores at the original locations of Al particles [43]. In cases where the TE reaction is highly intense, the released heat can damage the skeleton structure, leading to the formation of closed pores
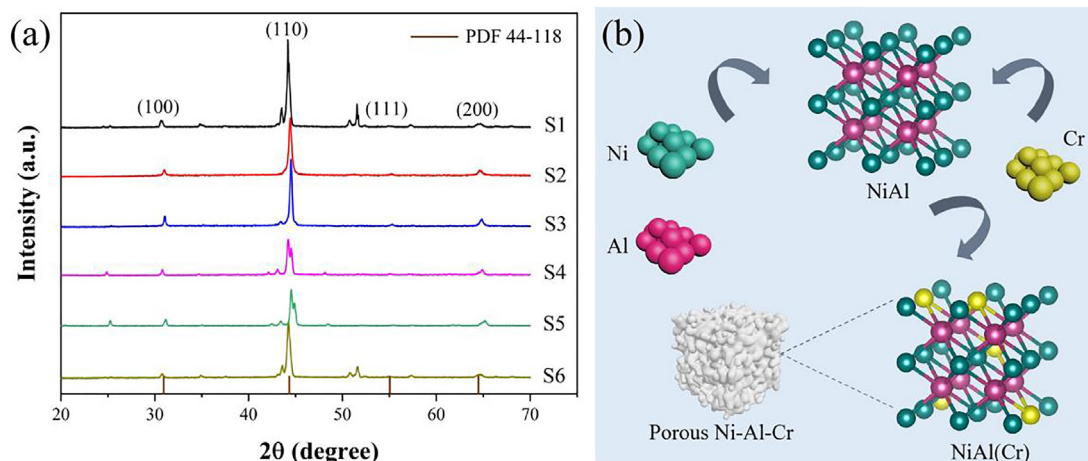
Fig. 8 − (a) XRD patterns of porous Ni−Al−Cr intermetallics in the β phase region. (b) The formation process of porous NiAl (Cr) substitutional solid solution.
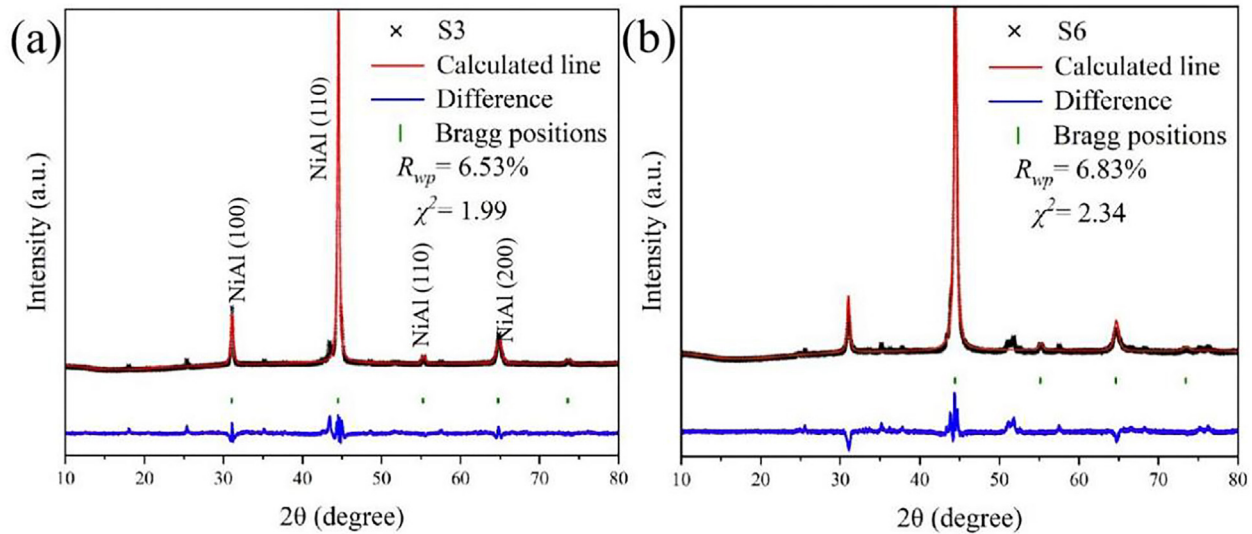
Fig. 9 — Rietveld refinement of XRD results of (a) S3 and (b) S6. The experimental data points are indicated by a black cross, the red line stands for the simulated diffraction pattern, a blue line represents the difference plot between the experimental and calculated results, and the green vertical bars label the position of the Bragg peaks of the NiAl phase. (For interpretation of the references to colour in this figure legend, the reader is referred to the Web version of this article.)

[11]. As the temperature gradually decreases after the TE reaction, volume shrinkage occurs upon solidification of the liquid phase, resulting in the formation of micropores within the skeleton structure [47]. Notably, the micropores may also contain Kirkendall pores due to differences in diffusion rates among the Ni, Al, and Cr elements, as depicted in Fig. S3 [26]. The Al-rich sample exhibits numerous connecting TE pores due to the intense TE reaction. Additionally, the particle surfaces have fewer atomic contact points, resulting in loosely aggregated powder particles without significant sintering neck formation. In contrast, the Al-poor sample displays a denser skeleton structure, and clear sintering necks formed through secondary crystallization can be observed. These sintering necks grow and become more viscous, leading to the disappearance of some micropores or their transformation into closed pores [48].

Fig. 11 shows the cross-section image of porous Ni—Al—Cr intermetallic compounds after polishing. In Fig. 11, the grey part represents the skeleton, and the black part is the pores. All Al-rich samples show uniformly distributed pores and have single-phase composition. From Fig. 12(a), the single-phase can be determined as β-NiAl phase. Compared with

Al-rich samples, an obvious diffusion layer can be observed in Al-poor samples. According to the point scanning result of Fig. 12(b—d), Ni, Cr, and Ni_5Al phase can be found, representing the result of an incomplete reaction [18]. Fig. 13 shows the map scanning result of the porous Ni—Al—Cr intermetallics. Obviously, Al-rich samples have a more uniform distribution of elements. The line scanning result of S6 is shown in Fig. S4. After holding at 1000 °C for 2 h, element Ni and Al are evenly distributed in the sintered product. Cr simple substance exists in the NiAl phase, due to its content exceeding the solid solubility. The Al-poor samples are difficult to form NiAl (Cr) substitutional solid solution. That is, intense TE reaction promotes the uniformity of element distribution.

The number of TE pores (between 38 μm and 74 μm) and micropores (smaller than 5 μm) in the porous Ni—Al—Cr intermetallics is calculated using Image J software,. and the results are presented in Fig. S5. In the Al-rich sample, the intense TE reaction facilitates the complete reaction of Al with Ni and Cr, leading to the formation of numerous TE pores. Remarkably, the number of micropores in S2 and S5 is lower compared to the other samples. It is worth noting that the

Table 2 — Rietveld refined structural parameters for porous Ni—Al—Cr intermetallic compounds.

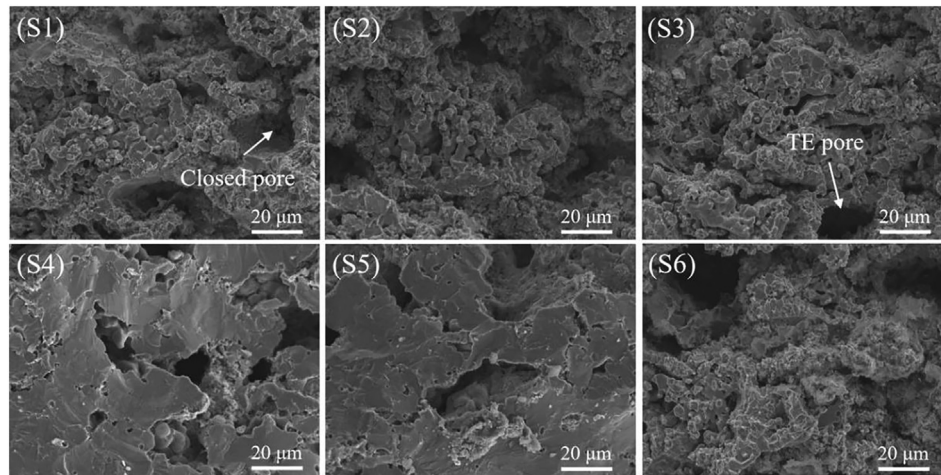| Alloy Composition	Lattice Parameters	Axial Ratio (c/a)	Unit Cell Volume (nm^3)	R-Factors (%)
42Ni—53Al—5Cr	$a_0 = 2.8879$ $b_0 = 2.8879$ $c_0 = 2.8879$ $\alpha = 90°, \beta = 90°, \gamma = 90°$	1	24.085	$Rwp = 6.53$ $\chi^2 = 1.99$
52Ni—43Al—5Cr	$a_0 = 2.8825$ $b_0 = 2.8825$ $c_0 = 2.8825$ $\alpha = 90°, \beta = 90°, \gamma = 90°$	1	23.949	$Rwp = 6.835$ $\chi^2 = 2.34$

Fig. 10 — SEM images of skeleton and pore morphology of porous Ni—Al—Cr intermetallics in the β phase region.

micropore includes the Kirkendall pore and blowhole. The interdiffusion coefficients of elements in ternary systems exhibit greater variations than those in binary systems. As a result, the number of micropores in S2 and S5 is lower in comparison to the other samples [18,44].

3.3. The compression property of porous Ni—Al—Cr in the β phase region

Compression tests are carried on to investigate the mechanical behaviour of porous Ni—Al—Cr intermetallics in the β phase region. The mixed powder was pressed into green compacts with a height of 20 mm and a diameter of 15 mm, following the requirements of the standard mechanical test sample. The resulting cylindrical samples were named CS1-CS6. The macroscopic morphology of corresponding sintered products is depicted in Fig. 14(b). Due to the violent TE reaction, noticeable pores appear on the surface of the Al-rich sample. CS1 and CS2 exhibit severe deformation, and CS3 shows cracks. Qualitatively evaluating the mechanical properties of Al-rich samples becomes challenging due to their

distorted morphology. Conversely, Al-poor samples maintain relatively intact morphology with stable pore structures. The stress-strain curves of CS3-6 after dynamic compression tests are illustrated in Fig. 14(a). All samples display evident elastic and fracture deformation regions, indicating the brittle fracture characteristics of the porous Ni—Al—Cr cylindrical samples. For brittle materials, the highest point on the stress-strain curves corresponds to the compressive strength [49]. The compressive strength of the Al-poor sample is better than that of the Al-rich sample. The maximum compressive strength is 538 MPa (CS5), and the minimum compressive strength is only 139 MPa, corresponding to CS3. Porosity has an important impact on the compression property of porous materials [50].

Compressive strength test results of CS3-6 are shown in Table S1. In three compression resistance tests, the difference in results is within an acceptable range. Fig. 15 shows the compressive strength comparison between four sample groups. CS4 and CS5 show excellent compressive resistance, which is related to the low porosity structure. The porosity of the porous Ni—Al—Cr cylindrical samples is determined
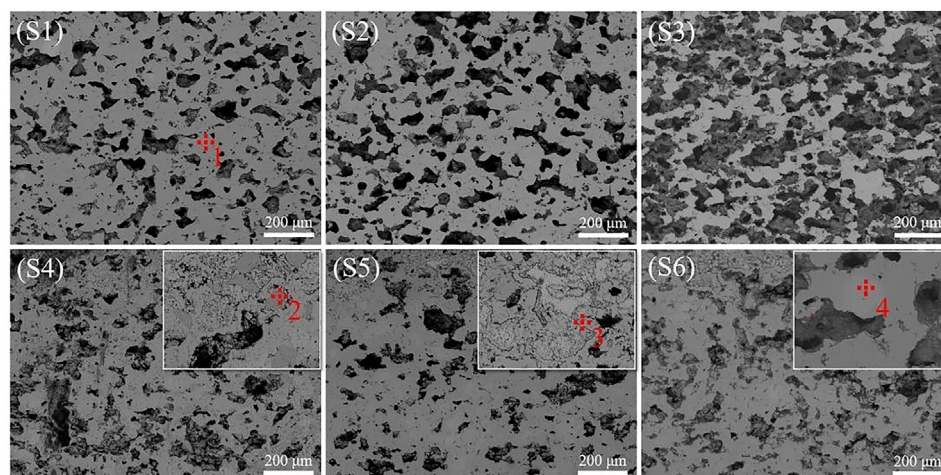
Fig. 11 — The cross-section micrographs of porous Ni—Al—Cr intermetallic compounds in the β phase region.
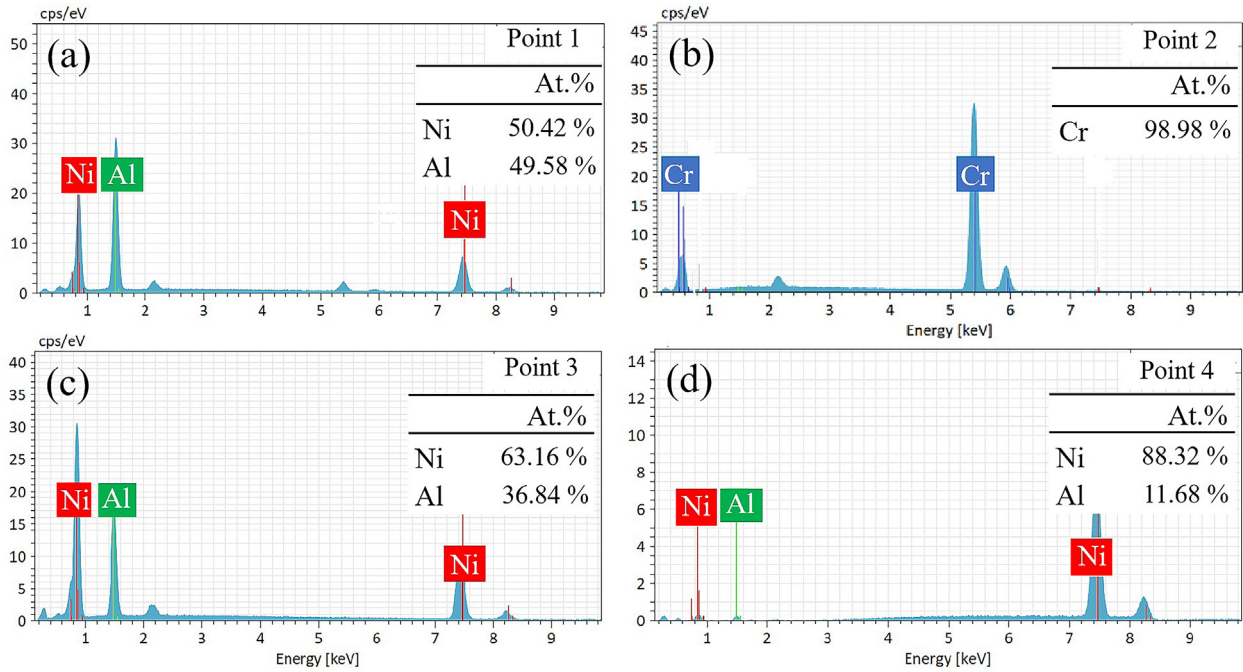
Fig. 12 − The corresponding point scanning results within Fig. 11(a-d) the result of point scanning of point 1−4.

using the Archimedes drainage method, and the results are presented in Fig. 16. In the Al-rich sample, the intense TE reaction leads to the formation of a highly porous structure, thereby weakening its mechanical properties. Conversely, low-porosity Al-poor samples demonstrate excellent compression resistance.

The relationship between compression strength and porosity of porous materials can be described by the Barsen equation [51], which is shown in Equation (8):

$$\sigma_b = \sigma_0 \times (1 - \theta)^m \tag{8}$$

Take the logarithm of both ends of Equation (8), and it can transform into Equation (9):

$$ln^{\sigma_b} = ln^{\sigma_b} + mln^{(1-\theta)} \tag{9}$$

σ_b is the strength of the porous materials. σ_0 is the constant, which is determined by the materials. m is a constant with values ranging from 2 to 6, related to the preparation process. θ is the porosity.

The functional relationship between porosity and yield stress of porous Ni−Al−Cr intermetallic is illustrated in Fig. 17(a). With increasing of porosity, the corresponding yield stress shows a decreasing trend. In CS5, the porosity is 17.02%, and the yield stress reaches the maximum value, which can reach 538 MPa. Fig. 17(b) shows the functional relationship between $ln (1-\theta)$ and $ln \sigma_b$, which can be fitted into linear relationships. The m and $ln \sigma_0$ can be calculated as 5.92 and 7.43, respectively. Thus, the quantitative relationship between porosity and strength of porous Ni−Al−Cr in the β phase region can be described as Equation (10). Actually, the yield stress is related to the number of TE
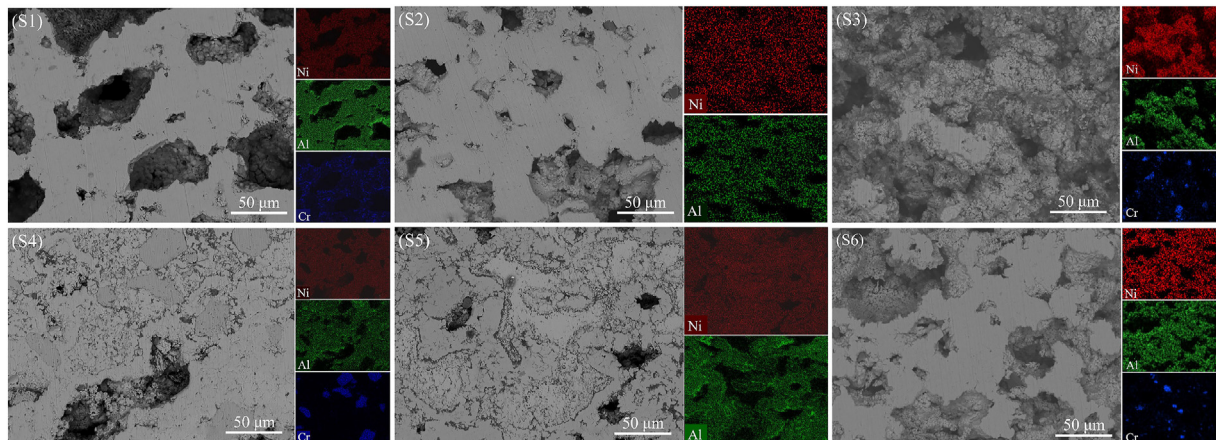
Fig. 13 − The map scanning analysis of the porous Ni−Al−Cr intermetallics.
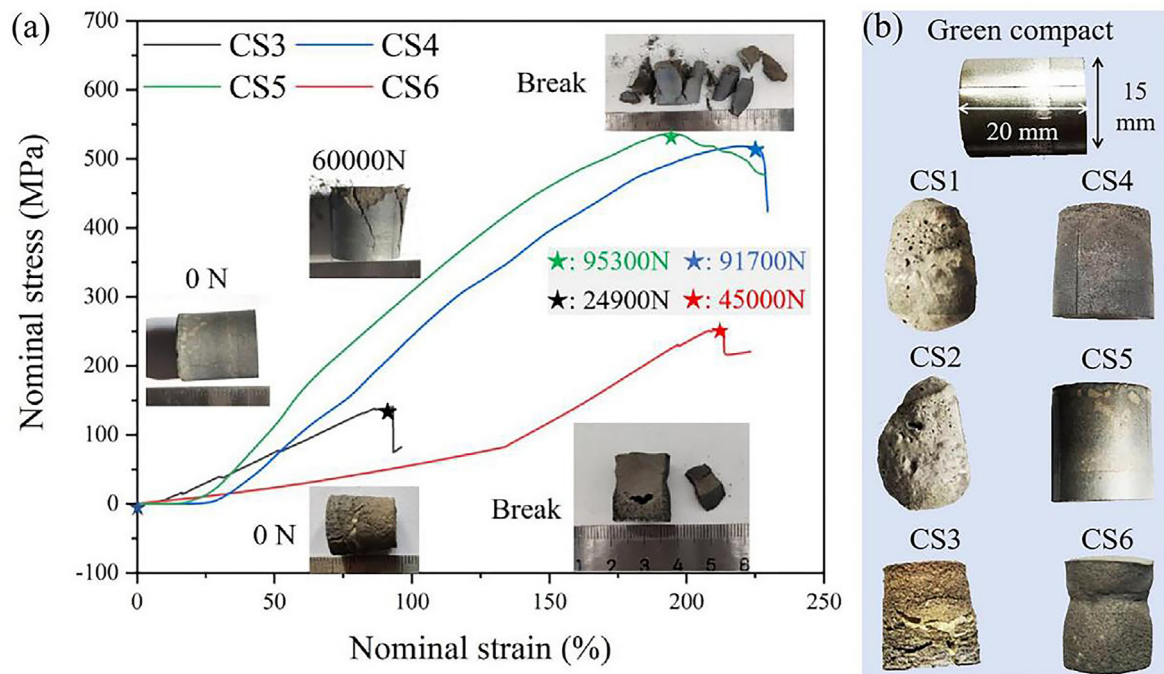
Fig. 14 − (a) Compression curves analysis of porous Ni−Al−Cr cylindrical samples in the β phase region. (b) The morphology of cylindrical green compact and sintered samples. (For interpretation of the references to colour in this figure legend, the reader is referred to the Web version of this article.)

pores (connecting pores), excessive TE pores can seriously reduce the mechanical properties of Ni−Al−Cr materials [52,53].

$$\sigma_b = 1685.8 \times (1 - \theta)^{5.92} \qquad (10)$$

To further investigate the fracture surface structure of porous Ni−Al−Cr cylindrical samples, the SEM images of fractured samples are shown in Fig. 18 (Al-rich cylindrical samples) and Fig. 19 (Al-poor cylindrical samples). Due to violent TE reaction occurs in Al-rich samples, many millimeter-

grade pores can be observed, in CS1 and CS2. During the TE reaction, the aggregated Al particles melt and form millimeter-grade pores. The high porosity structure decreases the compression property of porous Ni−Al−Cr cylindrical samples. In CS3, the strength of the pore walls is still weak, and the pore walls cause the cracks. In Al-poor cylindrical sample, the failure mode is a typical brittle cleavage fracture, and the yellow frame stands for the cleavage step. Compared with the Al-rich cylindrical sample, Al-poor cylindrical sample has lower porosity, and the fracture mode is mainly composed of transgranular cleavage [29].
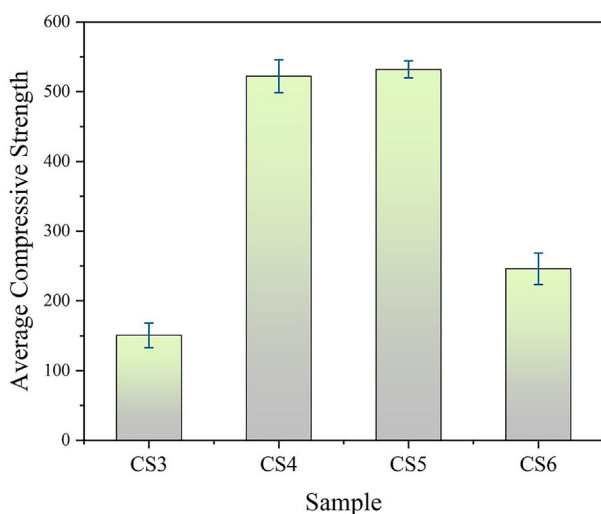
Fig. 15 − Compressive strength comparison between four sample groups.
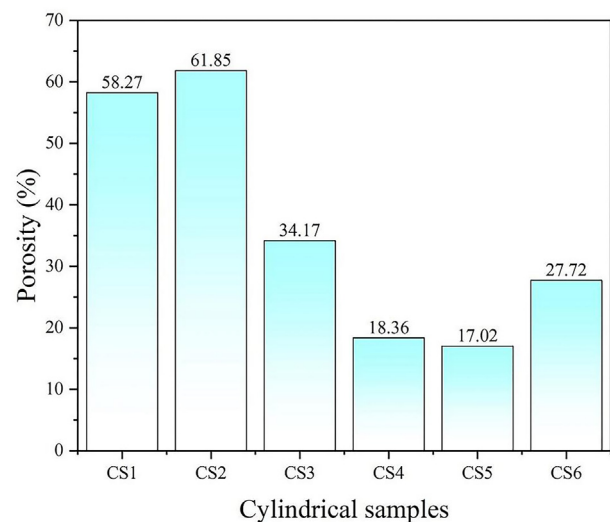
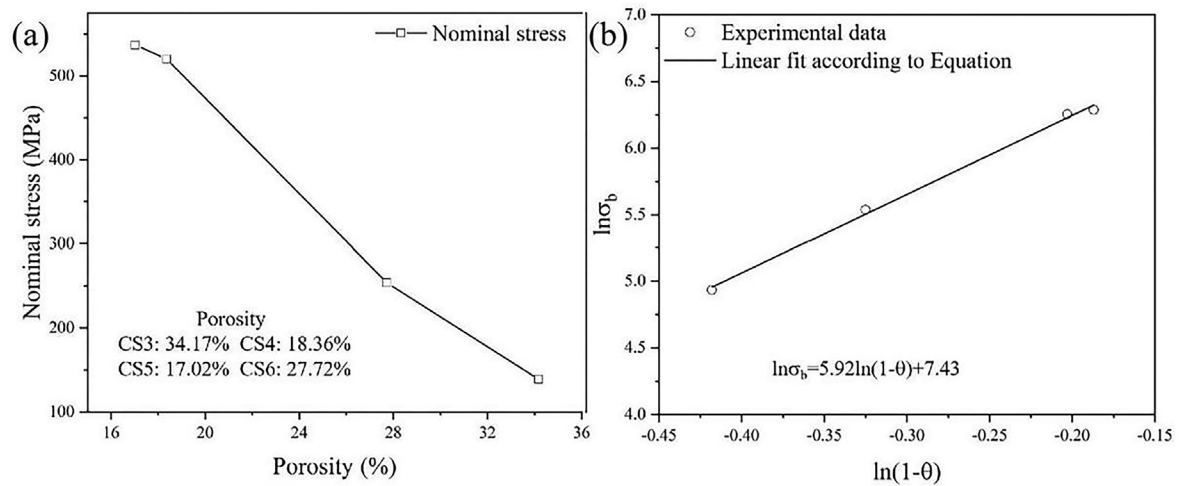**Fig. 16 − Porosity of the porous Ni−Al−Cr cylindrical samples.**

Fig. 17 — (a) Effect of porosity on nominal stress of cylindrical sintered samples in the β phase region. (b) Experimental verification of Barson equation for cylindrical sintered samples in the β phase region.

Fig. 20 shows the XRD patterns of porous Ni—Al—Cr cylindrical samples. The NiAl phase (β phase) is still the main phase, and other Cr—Al, and Ni—Al phases (Ni$_2$Al$_3$, NiAl$_3$) exist in the sample. With the size changes of the sample, the composition of porous Ni—Al—Cr can maintain stability.
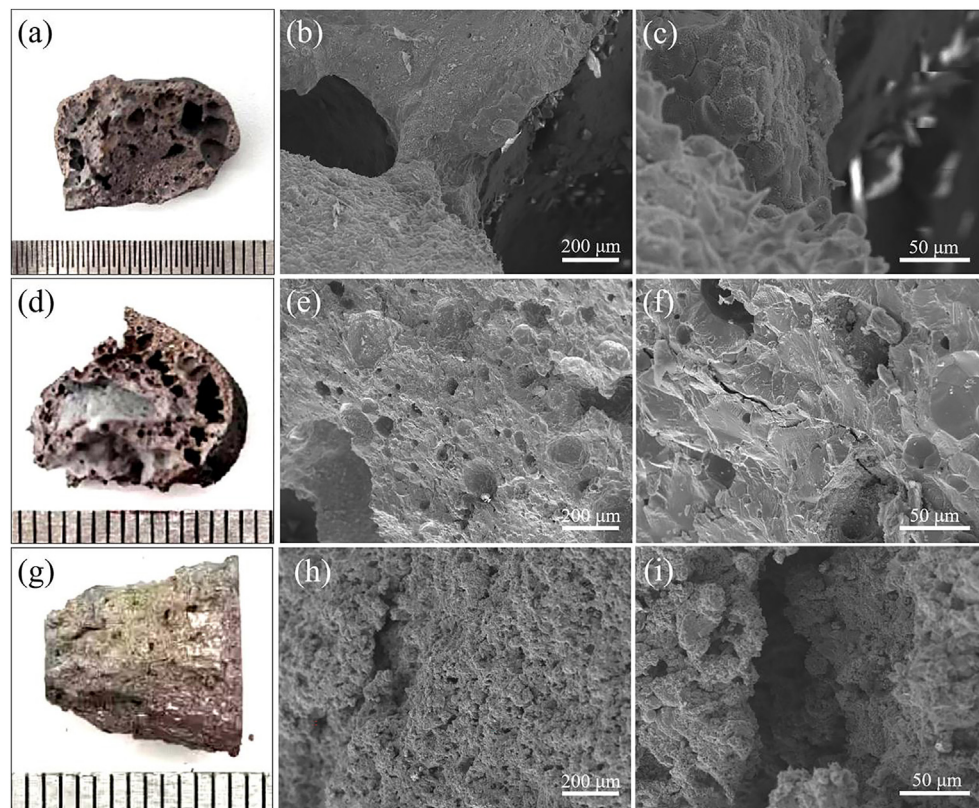

Fig. 18 — Macroscopic morphology and SEM images of CS1 (a—c), CS2 (d—f) and CS3 (g—i) in the β phase region after compression test.
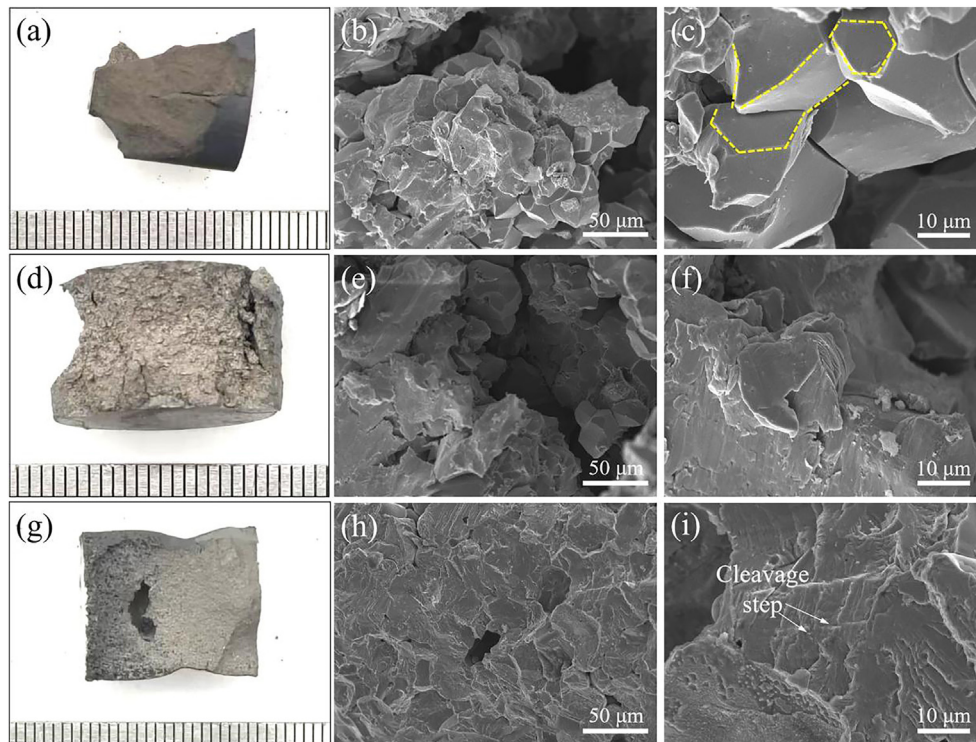
Fig. 19 − Macroscopic morphology and SEM images of CS4 (a−c), CS5 (d−f) and CS6 (g−i) in the β phase region after compression test.
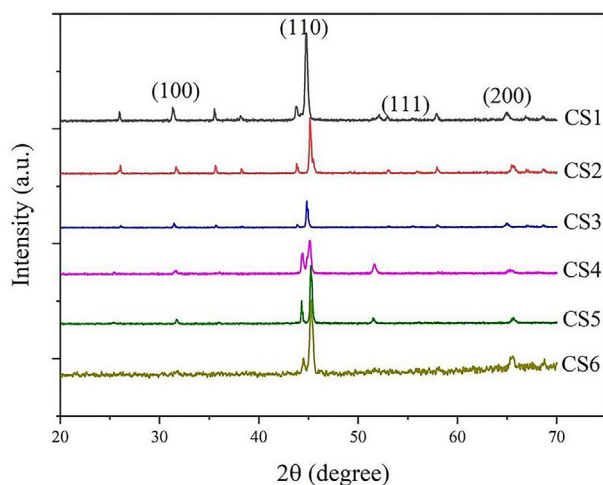
Fig. 20 − XRD pattern of porous Ni−Al−Cr cylindrical samples.

(1) During the TE reaction, the Ni−Al compounds (NiAl, Ni_2Al_3, Ni_3Al et al.) are prior to form, and Ni−Cr compounds ($AlCr_4$, Al_7Cr et al.) are hard to generate.

(2) Al content significantly influences the TE behaviour of porous Ni−Al−Cr intermetallics. Compared with the Al-poor sample, a more violent TE reaction occurs in the Al-rich sample. The Al-rich sample has a more obvious expansion effect (25.61%), higher porosity (44.39%), and can release more heat (1575 J g^{-1}).

(3) Violent TE reaction can promote the uniformity of the phase composition. From Rietveld refinement of the XRD pattern, the Al-rich sample tends to form uniform NiAl(Cr) substitutional solid solution.

(4) Porosity determines the compression resistance of porous Ni−Al−Cr intermetallics, high porosity structure decreases the strength of Ni−Al−Cr intermetallic compounds. Due to relatively low porosity, the Al-poor cylindrical sample shows fairly excellent compression resistance. The maximum yield stress of the sample can reach 538 MPa.

4.   Conclusions

Ni−Al−Cr intermetallics in β phase region with high porosity and excellent mechanical property were successfully prepared by thermal explosion (TE) reaction. The TE behaviour and compression resistance in the β phase region were investigated. Conclusions can be summarized as follows.

Credit authorship contribution statement

Yang Yu: Data curation, Formal analysis, Visualization, Writing- original draft. **Baojing Zhang**: Methodology, Supervision. **Xiaoping Cai**: Conceptualization, Methodology, Supervision. **Zhejian Cao**: Writing - review & editing. **Farid Akhtar**: Formal analysis. **Xinyang Jiao**: Conceptualization,

Methodology, Supervision, Writing - review & editing. **Xueding Chai**: Formal analysis. **Peizhong Feng**: Conceptualization, Funding acquisition, Methodology, Supervision.

Data availability

The raw/processed data required to reproduce these findings cannot be shared at this time as the data also forms part of an ongoing study.

Declaration of competing interest

The authors declare that they have no known competing financial interests or personal relationships that could have appeared to influence the work reported in this paper.

Acknowledgments

Appendix A. Supplementary data

Supplementary data to this article can be found online at https://doi.org/10.1016/j.jmrt.2023.06.173.

REFERENCES

[1] Carneiro LD, de Vasconcelos SF, Neto GWD, Brito RP, Brito KD. Improving H_2S removal in the coke oven gas purification process. Separ Purif Technol 2021;257:117862. https://doi.org/10.1016/j.seppur.2020.117862.

[2] Chen YJ, Yao KN, Zhang X, Shen BX, Jr RLS, Guo HX. Siloxane-modified MnOx catalyst for oxidation of coal-related o-xylene in presence of water vapor. J Hazard Mater 2022;436:129109. https://doi.org/10.1016/j.jhazmat.2022.129109.

[3] Li F, Chu MS, Tang J, Liu ZG, Zhou YS, Wang JX. Exergy analysis of hydrogen-reduction based steel production with coal gasification-shaft furnace-electric furnace process. Int J Hydrogen Energy 2021;46:12771—83. https://doi.org/10.1016/j.ijhydene.2021.01.083.

[4] Wang LY, An L, Zhao J, Shimai S, Mao XJ, Zhang J, Liu J, Wang SW. High-strength porous alumina ceramics prepared from stable wet foams. Journal of Advanced Ceramics 2021;10:852—9. https://doi.org/10.1007/s40145-021-0479-9.

[5] Dilip JJS, Miyanaji H, Lassell A, Starr TL, Stucker B. A novel method to fabricate TiAl intermetallic alloy 3D parts using additive manufacturing. Defence Technology 2017;13:72—6. https://doi.org/10.1016/j.dt.2016.08.001.

[6] Fursenko R, Maznoy A, Odintsov E, Kirdyashkin A, Minaev S, Sudarshan K. Temperature and radiative characteristics of cylindrical porous Ni-Al burners. Int J Heat Mass Tran 2016;98:277—84. https://doi.org/10.1016/j.ijheatmasstransfer.2016.03.048.

[7] Chen SL, Wang L, He G, Li JT, Wang CA. Microstructure and properties of porous Si3N4 ceramics by gelcasting-self-propagating high-temperature synthesis (SHS). Journal of Advanced Ceramics 2022;11:172—83. https://doi.org/10.1007/s40145-021-0525-7.

[8] Wang XF, Li ZD, Huang YJ, Wang K, Wang XF, Han FS. Processing of magnesium foams by weakly corrosive and highly flexible space holder materials. Mater Des 2014;64:324—9. https://doi.org/10.1016/j.matdes.2014.07.049.

[9] Srivastava N, Chaudhari GP. Effect of ultrasonic treatment on the mechanical behaviour of Al-Ni alloys. Mater Sci Technol 2019;35:1239—47. https://doi.org/10.1080/02670836.2019.1618621.

[10] Shaga A, Shen P, Sun C, Jiang QC. Lamellar-interpenetrated Al-Si-Mg/SiC composites fabricated by freeze casting and pressure less infiltration. Mater Sci Eng, A 2022;630:78—84. https://doi.org/10.1080/02670836.2019.1618621.

[11] Yu Y, Cai XP, Cao ZJ, Jiao XY, Xie WN, Yu Y, Feng PZ. Effect of the heating rate on the thermal explosion behavior and oxidation resistance of 3D-structure porous NiAl intermetallic. Mater Char 2022;190:112062. https://doi.org/10.1016/j.matchar.2022.112062.

[12] Shu YM, Suzuki A, Takata N, Kobashi M. Fabrication of porous NiAl intermetallic compounds with a hierarchical open-cell structure by combustion synthesis reaction and space holder method. J Mater Process Technol 2019;264:182—9. https://doi.org/10.1016/j.jmatprotec.2018.09.010.

[13] Geramifard G, Gombola C, Franke P, Seifert HJ. Oxidation behaviour of NiAl intermetallics with embedded Cr and Mo. Corrosion Sci 2020;177:108956. https://doi.org/10.1016/j.corsci.2020.108956.

[14] He J, Luan Y, Guo HB, Peng H, Zhang YL, Zhang T, Gong SK. The role of Cr and Si in affecting high-temperature oxidation behavior of minor Dy doped NiAl alloys. Corrosion Sci 2013;77:322—33. https://doi.org/10.1016/j.corsci.2013.08.020.

[15] Hu XL, Zhang Y, Lu GH, Wang TM. Role of the alloying element in suppressing the negative effect of O in NiAl: Cr as an example. Scripta Mater 2009;61:189—92. https://doi.org/10.1016/j.scriptamat.2009.03.041.

[16] Zhao JC, Zheng X, Cahill DG. Thermal conductivity mapping of the Ni-Al system and the beta-NiAl phase in the Ni-Al-Cr system. Scripta Mater 2012;66:935—8. https://doi.org/10.1016/j.scriptamat.2012.02.035.

[17] Grushko B, Kowalski W, Pavlyuchkov D, Przepiorzynski B, Surowiec M. A contribution to the Al-Ni-Cr phase diagram. J Alloys Compd 2008;460:299—304. https://doi.org/10.1016/j.jallcom.2007.06.044.

[18] Yu Y, Cai XP, Jiao XY, Xu CY, Niu JN, Feng PZ. Oxidation resistance at 900 °C of porous Ni-Al-Cr intermetallics synthesized via rapid thermal explosion reaction. J Alloys Compd 2022;906:164374. https://doi.org/10.1016/j.jallcom.2022.164374.

[19] Raghavan V. Al-Cr-Ni (Aluminum-Chromium-Nickel). J Phase Equilibria Diffus 2008;30:61—3. https://doi.org/10.1007/s11669-008-9437-2.

[20] Ukai S, Yano Y, Inoue T, Sowa T. Solid-solution strengthening by Al and Cr in FeCrAl oxide-dispersion-strengthened alloys. Mater Sci Eng, A 2021;812:141076. https://doi.org/10.1016/j.msea.2021.141076.

[21] Shao ZY, Jiang XS, Shu R, Wu ZX, Huang ZG, Deng H, Qin Q, Zhu MH. Effect of Cr micro-alloying on microstructure and mechanical properties of alumina whisker and graphene co-reinforced copper matrix composites. J Alloys Compd 2022;909:164804. https://doi.org/10.1016/j.jallcom.2022.164804.

[22] Wei YZ, Qiu F, Shu SL, Tong HT, Yang HY, Jiang QC. Microstructure manipulation and strengthening mechanism of TiAl composites reinforced by Cr solid solution and in-situ

nanometer-sized TiB_2 particles. Mater Sci Eng, A 2022;845:143214. https://doi.org/10.1016/j.msea.2022.143214.

[23] Jiang H, Ye SL, Ma R, Yu P. Influences of sintering parameters on shape-retention ability of porous Ni_3Al intermetallic fabricated by powder metallurgy. Intermetallics 2019;105:48–55. https://doi.org/10.1016/j.intermet.2018.11.009.

[24] Wang Z, Jiao XY, Feng PZ, Wang XH, Liu ZS, Akhtar F. Highly porous open cellular TiAl-based intermetallics fabricated by thermal explosion with space holder process. Intermetallics 2016;68:95–100. https://doi.org/10.1016/j.intermet.2015.09.010.

[25] Karczewski K, Stepniowski WJ, Salerno M. Amino acids aided sintering for the Formation of highly porous FeAl intermetallic alloys. Materials 2017;10:746–54. https://doi.org/10.3390/ma10070746.

[26] Jiao XY, Feng PZ, Wang JZ, Ren XR, Akhtar F. Exothermic behavior and thermodynamic analysis for the formation of porous $TiAl_3$ intermetallics sintering with different heating rates. J Alloys Compd 2019;811:152056. https://doi.org/10.1016/j.jallcom.2019.152056.

[27] Karczewski K, Stepniowski WJ, Salerno M. Fabrication of FeAl intermetallic foams by tartaric acid-assisted self-propagating high-temperature synthesis. Materials 2018;11:621. https://doi.org/10.3390/ma11040621.

[28] Dong HX, He YH, Jiang Y, W L, Zou J, Xu NP, Huang BY, Liu CT. Effect of Al content on porous Ni-Al alloys. Mater Sci Eng, A 2011;528:4849–55. https://doi.org/10.1016/j.msea.2011.02.014.

[29] Cai XP, Feng PZ. Reaction mechanism and oxidation resistance at 700-900 °C of high porosity NiAl intermetallic. Corrosion Sci 2021;191:109731. https://doi.org/10.1016/j.corsci.2021.109731.

[30] Jiao XY, Liu YN, Cai XP, Wang JZ, Feng PZ. Progress of porous Al-containing intermetallics fabricated by combustion synthesis reactions: a review. J Mater Sci 2021;56:11605–30. https://doi.org/10.1007/s10853-021-06035-5.

[31] Jiao XY, Wang XH, Kang XQ. Rapid reactive synthesis of $TiAl_3$ intermetallics by thermal explosion and its oxidation resistance at high temperature. Prog Nat Sci: Mater Int 2016;32:489–94. https://doi.org/10.1016/j.pnsc.2019.05.002.

[32] Cai XP, Liu YN, Feng PZ, Jiao XY, Zhang LQ, Wang JZ. Fe-Al intermetallic foam with porosity above 60 % prepared by thermal explosion. J Alloys Compd 2018;732:443–7. https://doi.org/10.1016/j.jallcom.2017.10.228.

[33] Cai XP, Xu R, R XR, Kang XQ, Feng PZ. Microstructure and oxidation resistance of porous $NbAl_3$ intermetallic prepared by thermal explosion reaction. Mater Sci Technol 2019;35:1624–31. https://doi.org/10.1080/02670836.2019.1635739.

[34] Xu F, Xiao Y, Hu X, Dong B, Liu W, Li Y. In situ investigation of Al-Ti mixed metal system microwave sintering by synchrotron radiation computed tomography. J Instrum 2016;11:C02074. https://doi.org/10.1088/1748-0221/11/02/c02074.

[35] Yu TM, Jiang FC, Wang CH, Cao MX, Wang ZQ, Chang YP, Guo CH. Investigation on fabrication and microstructure of Ti-6Al-4V alloy hollow spheres by Powder Metallurgy, Metals and Materials International 2021;27:1083–91. https://doi.org/10.1007/s12540-019-00462-5.

[36] Xie L, Chen XF, Zhao NR, Guo CL. Study on porous bioglass scaffold prepared by dipping with polymer foams. J Inorg Mater 2009;24:280–4. https://doi.org/10.3724/sp.j.1077.2009.00280.

[37] Agbedor SO, Yang DH, Chen JQ, Wang L, Wu H. Low-temperature reactive sintered porous Mg-Al-Zn alloy foams. Metals 2022;12. https://doi.org/10.3390/met12040692.

[38] Shirani Bidabadi AR, Enayati MH, Dastanpoor E, Varin RA, Biglari M. Nanocrystalline intermetallic compounds in the Ni-Al-Cr system synthesized by mechanical alloying and their thermodynamic analysis. J Alloys Compd 2013;581:91–100. https://doi.org/10.1016/j.jallcom.2013.07.037.

[39] Jin LL, Kevorkov D, Medraj M, Chartrand P, Al-Mg -RE, Re= La, Ce Pr, Nd Sm. systems: thermodynamic evaluations and optimizations coupled with key experiments and Miedema's model estimations. J Chem Therm 2013;58:166–95. https://doi.org/10.1016/j.jct.2012.10.021.

[40] Ray PK, Akinc M, Kramer MJ. Applications of an extended Miedema's model for ternary alloys. J Alloys Compd 2010;489:357–61. https://doi.org/10.1016/j.jallcom.2009.07.062.

[41] Cai HS, Guo F, Su J, Liu L. Thermodynamic analysis of Al-re phase formation in AZ91-RE (Ce, Y, Gd) magnesium alloy. Physica Status Solidi (b) Basic Solid State Physics 2019;257:1900453. https://doi.org/10.1002/pssb.201900453.

[42] Zhang RF, Zhang SH, He ZJ, Jing J, Sheng SH. Miedema Calculator: a thermodynamic platform for predicting formation enthalpies of alloys within framework of Miedema's Theory. Comput Phys Commun 2016;209:58–69. https://doi.org/10.1016/j.cpc.2016.08.013.

[43] Wen X, Huang BS, Xie YJ, Luo X. Preparation and properties of porous Fe-Al-x%TiC composite material. J Mater Eng Perform 2022. https://doi.org/10.1007/s11665-022-06835-z.

[44] Zhang HB, Gao HY, Yu H, Wang LF, Liu XL, Ma JL, Zhang NH, He YH, Jiang Y. The role of Cr in the reactive synthesis of porous FeAlCr intermetallic compounds. Mater Chem Phys 2020;249:123013. https://doi.org/10.1016/j.matchemphys.2020.123013.

[45] Agbedor SO, Yang DH, Chen JQ, Wang L, Wu H. Low-temperature reactive sintered porous Mg-Al-Zn alloy foams. Metals 2022;12. https://doi.org/10.3390/met12040692.

[46] Jiang Y, He YH, Gao HY. Recent progress in porous intermetallics: synthesis mechanism, pore structure, and material properties. J Mater Sci Technol 2021;74:89–104. https://doi.org/10.1016/j.jmst.2020.10.007.

[47] Padalko AG, Ellert OG, Efimov NN, Novotortsev VM, Talanova GV, Zubarev GI, Fedotov VT, Suchkov AN, Solntsev KA. Barothermal analysis of phase transformations of an Al-15 at % Ni alloy and its structure and magnetic properties. Inorg Mater 2013;49:1091–7. https://doi.org/10.1134/s0020168513110113.

[48] Zhang HB, Wang LF, Ma JL, Yu H, Xu SH, Hou GY, He YH, Zheng GQ. Reactive synthesis of porous FeAlCr intermetallics with enhanced mechanical property and oxidation resistance by introducing yttrium borides. Mater Chem Phys 2021;273:124929. https://doi.org/10.1016/j.matchemphys.2021.124929.

[49] Lee JW, Hyun SK, Kim MS, Kim MG, Ide T, Nakajima H. Elevated temperature compression behaviors of lotus-type porous NiAl. Intermetallics 2012;29:27–34. https://doi.org/10.1016/j.intermet.2012.04.010.

[50] Wang H, Su MM, Hao H. Compressive properties and energy absorption behavior of Mg17Al12/Al ordered structure composites. Composites Part B 2021;210:108688. https://doi.org/10.1016/j.compositesb.2021.108688.

[51] Zhang HB, Ma JL, Gao ZC, Guo F, Xu SH, Hou GY, Zheng ZQ. Study on stability of mechanical properties for porous Fe-Cr-Al alloys after long-term aging. Materials 2022;15:3718. https://doi.org/10.3390/ma15103718.

[52] Nie HC, Yu Y, Liu YS, He HL, Wang GS, Dong XL. Enhanced shock performance by disperse porous structure:A case study in PZT95/5 ferroelectric ceramics. J Am Ceram Soc 2017;100:5693–9. https://doi.org/10.1111/jace.15097.

[53] Shivaram MJ, Arya SB, Nayak J, Panigrahi BB. Electrochemical corrosion and impedance studies of porous Ti-xNb-Ag alloy in physiological solution. Trans Indian Inst Met 2020;73:921–8. https://doi.org/10.1007/s12666-020-01904-0.